



Simulation and experimental comparison of the thermo-mechanical history and 3D microstructure evolution of 304L stainless steel tubes manufactured using LENS

Kyle L. Johnson¹ · Theron M. Rodgers² · Olivia D. Underwood² · Jonathan D. Madison² · Kurtis R. Ford² · Shaun R. Whetten² · Daryl J. Dagle² · Joseph E. Bishop²

Received: 15 September 2017 / Accepted: 14 November 2017 / Published online: 2 December 2017
© Springer-Verlag GmbH Germany, part of Springer Nature (outside the USA) 2017

Abstract

Additive manufacturing enables the production of previously unachievable designs in conjunction with time and cost savings. However, spatially and temporally fluctuating thermal histories can lead to residual stress states and microstructural variations that challenge conventional assumptions used to predict part performance. Numerical simulations offer a viable way to explore the root causes of these characteristics, and can provide insight into methods of controlling them. Here, the thermal history of a 304L stainless steel cylinder produced using the Laser Engineered Net Shape process is simulated using finite element analysis (FEA). The resultant thermal history is coupled to both a solid mechanics FEA simulation to predict residual stress and a kinetic Monte Carlo model to predict the three-dimensional grain structure evolution. Experimental EBSD measurements of grain structure and in-process infrared thermal data are compared to the predictions.

Keywords Additive manufacturing · LENS · Microstructure · Columnar · Equiaxed · EBSD · Thermal simulation · Residual stress · Kinetic Monte Carlo

1 Introduction

Additive Manufacturing (AM) is a broad term that describes the fabrication of parts by the addition of material and generally excludes material removal processes as is done in other machining techniques [1]. AM methods exist for many different material types including metals, ceramics, and polymers. Within the domain of metals, most AM processes can be separated into two major groups that are classified as directed energy deposition (DED) and powder bed fusion (PBF). In PBF techniques, a pre-placed bed of powder is selectively melted by a heat source, typically a laser or electron beam. After the heat source completes the scan for the current layer, a thin layer of powder is placed on top of the existing layer by a roller or blade, and the process is repeated until the part is complete. PBF techniques often provide better surface finish,

but can be time-intensive due to the small beam diameters and powder layers used [1]. In contrast, DED methods feed material into the laser beam in the form of wire feedstock or powder blown into the beam by nozzles using a carrier gas [2,3]. These techniques are often used for building larger parts rapidly [4] and for the repair of parts subjected to wear that would not be repairable through powder bed techniques [1]. One of the most common DED methods is the Laser Engineered Net Shape (LENS) process [5], which uses multiple nozzles to blow metal powder into a vertical laser beam onto a movable baseplate. The current study focuses on predicting the thermo-mechanical history and three-dimensional microstructure evolution of a 304L stainless steel tube produced using the LENS technique.

While AM offers immense opportunities for rapid production of complex geometries with potentially tailored microstructures and mechanical properties, part qualification remains a challenge, particularly for critical parts [1,6]. A key concern is the presence of defects such as porosity and lack of fusion. Additionally, residual stress can be detrimental to part performance and must be minimized [7]. Physics-based process models are becoming sufficiently advanced to allow for the development of computational defect indica-

✉ Kyle L. Johnson
kyljohn@sandia.gov

¹ Sandia National Laboratories, PO Box 5800, MS 0346,
Albuquerque, NM 87185, USA

² Sandia National Laboratories, PO Box 5800, Albuquerque,
NM 87185, USA

tors and optimization of the residual-stress field. Recently, much attention has been given to accurately modeling the AM process using finite element methods [8–12]. Numerical heat transfer methods have been in use for decades, but AM processes present a new challenge since material is constantly added to the system at the location of intense thermal gradients and phase changes. A common approach to modeling the thermal aspect of AM processes involves moving a heat source around a finite element mesh with temperature dependent thermal properties and some form of activation mechanism, such as a scale factor on thermal conductivity and specific heat once a threshold temperature is reached, that specifies when a material has been melted. The heat source often possesses a Gaussian form and can be either surface-based or volumetric [13].

Effort has also been given to predict microstructures resulting from AM processes, both experimentally and numerically. Dehoff et al. [14] recently demonstrated that by manipulating process parameters, microstructures could be controlled to yield single crystals parallel to the build direction, relatively equiaxed grains, or grains with texture oriented transverse to build directions. Bontha et al. [15] used numerical techniques to investigate solidification microstructures in Ti–6Al–4V structures. The authors calculated thermal gradient (G) and solidification velocity (R) values using the Rosenthal equation for LENS builds and found that microstructure can transition from columnar to equiaxed at higher powers. Vastola et al. [16] and Kelly and Kampe [17] performed 2D modeling on the phase formation and transformation of Ti–6Al–4V during LPBF processes. Roehling et al. used numerical simulations to investigate solidification in comparison to experimental microstructures, and found that changing melt pool shape altered the solidification microstructure. Francois et al. provided an extensive survey of the most recent advances in microstructure modeling for AM processes ranging from the mesoscale to the macroscale. It was shown that while a variety of tools are emerging, very few examples span length scales while simultaneously using process models to predict both microstructure and properties [11]. The objective of this work is to advance the capabilities necessary to predict the process-structure-property-performance relationships of AM parts. To this end, the thermal, structural (residual stress), and microstructural histories have been predicted for a 304L stainless steel cylinder. Experimental comparison to the simulations is also provided and discussed.

2 Methods and materials

A 304L stainless steel cylinder with a height of 50 mm and an outside diameter of 24 mm was chosen for this study. The cylinder was built by the LENS process using a cir-

cular raster pattern. The thermal-structural analysis of the tube consisted of one-way coupled thermal and mechanical simulations using the finite element method. The thermal simulation was performed first, and the resulting transient temperature field was then used to drive the mechanical simulation to predict the residual stress field. Homogenized isotropic material properties were used for both the thermal and mechanical simulations. The effect of material texture (preferred grain orientations) on the mechanical response (both elastic and plastic) is an active area of research, but will not be discussed here. The nonlinear heat-transfer model is described in Sect. 2.2. The nonlinear solid mechanics simulation is described in Sect. 2.3. Both the thermal and structural simulations were performed using the Sierra multiphysics finite-element software suite [18].

The transient-temperature field was also used in a kinetic Monte Carlo (KMC) simulation to generate the microstructure morphology. The KMC-based microstructure prediction was performed using the Stochastic Parallel Particle Kinetic Simulator (SPPARKS—<http://spparks.sandia.gov>) [19]. Although outside the scope of this paper, we note that the predicted microstructure could be used in a mechanical simulation of the tube using crystal-plasticity constitutive models [20], simulating both the additive process through cooldown as well as structural performance.

2.1 LENS build

The cylinder was built using a custom LENS machine developed at Sandia National Labs. The focused laser beam diameter used in this study deviated from typical LENS parameters so that the full thickness of the wall could be built in a single pass. The 4 mm laser diameter initially required 2000 W to ensure good metallurgical bonding to the 304 stainless steel baseplate. As the cylinder grew, less energy was required to provide complete melting of the powder than in the lower layers of the part. As a result, the laser power was ramped down in 250 W increments every 4.5 mm of build height, or 5 layers, until the power reached 1250 W. The power was held constant after this final drop, which corresponded to a vertical height of 13.5 mm. These drops in power prevented excessive heat buildup in the tube, which could lead to an increased wall thickness due to slump, and allowed the walls to build at a more uniform thickness. The metal powder that was used in this study was nitrogen atomized 304L stainless steel powder with a 44–106 micron size distribution. This powder was carried to the print head at a rate of 18 g/min using an argon carrier gas flowing at 1.6 l/min. The powder incorporation efficiency has not been measured, but is estimated to be greater than 20%. The laser speed was 400 mm/min. The resulting as-built part can be seen in Fig. 1 while still attached to the baseplate.



Fig. 1 Side view of as-built 304L LENS tube. The individual layers are clearly visible, as well as some discoloration due to the heat up of the tube during the build. The tube had a 50 mm height, 16 mm inside diameter, and 24 mm outside diameter

2.2 Thermal prediction

The transient temperature field of the LENS process was simulated by scanning a Gaussian heat source across a pre-existing finite-element mesh at the nominal velocity provided in Sect. 2.1. The trajectory of the hot spot was prescribed by a text file (i.e. path file) used by the LENS machine in G-code format. Finite elements were activated by prescribing an increase in thermal conductivity as the elements reached the melting temperature of the material. This approach allows for the simulation of both PBF and DED fabrication methods. For simulations of a PBF process, such as selective laser melting, the inactive elements initially have a thermal conductivity corresponding to the value of the powder. For simulations of a DED process, such as LENS, the inactive elements have zero thermal conductivity. Once they are activated, the conductivity becomes the temperature-dependent value of the bulk material. While inactive elements have zero thermal conductivity, the energy equation is solved for all elements at all times. Energy is added by the volumetric source term when the elements are being traversed by the source, thereby heating the elements and increasing the temperature. If the elements receive enough heat from the source term to reach melting temperature, they are then activated. This numerical method does not directly consider the powder flow rate through mass addition. Instead, we assume that any material addition is captured by the volume of elements that are activated by the heat source. This assumption is linked to the experiment by matching the layer height and deposition width of the model to that of the experiment. Because a

Table 1 Temperature dependent properties used in thermal FEA from Bogaard et al. [58]

Temperature (K)	C_p (J/kg)	k (W/m/K)
300	480	14.8
476	–	17.65
600	550	–
675	–	20.7
774	–	21.4
881	–	23.5
973	–	24.5
1075	–	25.8
1175	–	27.5
1278	–	28.8
1377	–	30
1400	675	–
1476	–	31.4
1550	693	–
1574	–	32.7
1650	714	–
1673	–	33.6
1750	736	–

Properties in between listed temperatures were interpolated in a linear manner. Properties above the highest listed values were assumed constant

change in powder feed rate would cause a change in the experimentally deposited geometry, i.e. thicker or thinner layers and/or different material deposition width, we assume that this approach adequately represents the process.

During the thermal process, the heat transfer energy is solved according to the following governing equation:

$$\rho C_p \frac{\partial T}{\partial t} = -\nabla \cdot (-k\nabla T) + H_v \tag{1}$$

where ρ is the material density, C_p is the specific heat, T is the temperature, q is the heat flux, and H_v is the laser heat source. Convection and radiation are calculated on the free surfaces of the part as described by Eqs. (2) and (3), respectively,

$$q = h(T - T_\infty) \tag{2}$$

$$q = \epsilon \sigma (T^4 - T_r^4) \tag{3}$$

where h is the convection coefficient, ϵ is the emissivity, σ is the Stefan–Boltzmann constant, and T_∞ and T_r are both taken as room temperature. In this analysis density and emissivity were held constant at 7609 kg/m^3 and 0.4, respectively. Table 1 contains the temperature dependent thermal properties used in the simulation. Because the powder is melted immediately upon entering the laser beam in a LENS process and mass flow into the beam was not explicitly modeled

Table 2 Constant properties used in thermal FEA

Parameter	Value
Ambient temperature, T_∞ (K)	298
Convection coefficient, h ($\text{W}/\text{m}^2 \text{K}$)	25
Emissivity, ϵ	0.4
Latent heat, H (J/kg)	285,000
Density, ρ (kg/m^3)	7609
Laser efficiency	0.47
Laser diameter, d (mm)	4
Laser velocity, v (mm/s)	6.67
Laser power (W)	1250–2000 (see thermal analysis section)
Solidus temperature, T_s (K)	1673
Liquidus temperature, T_l (K)	1723

here, only bulk material properties were considered. Due to the forced convection on the tube surface caused by the powder carrier gas and laser shield gas, a convection coefficient of 25.0 was applied to the tube free surfaces and the top of the baseplate. This approach mirrors that of Heigel et al. [21]. The constant material properties are listed in Table 2. The latent heat of fusion is applied to the specific heat in a uniform manner across the temperature range from the solidus temperature to the liquidus temperature. The simulations were solved in an implicit manner with a constant time step as reported in [22], where simulation time evolved according to the formula

$$\tau_i = \tau_{i-1} + \frac{d}{2 * v} \quad (4)$$

where d is the laser diameter and v is the laser velocity. The time step formulation in Eq. (4) which is added to the previous time τ_{i-1} is necessary due to the FE solution process. With this formulation, the thermal equations will be solved at a maximum distance of the laser radius from the previous time step. A time step larger than this may skip over elements when calculating heat input, depending on the mesh size. This jump in heat input can cause the appearance of a pulsed heat source and lead to highly erroneous temperature values.

The mesh used in the simulations is shown in Fig. 2 below. The mesh consisted of 492,268 hexahedral elements. The baseplate mesh was coarsened away from the cylinder to lower the element count. The build time of approximately 577 s was simulated, followed by a cooldown for a total time of 1000 s.

2.3 Residual stress prediction

Once the thermal simulation is complete, the temperature history of the mesh serves as an input to the solid mechanics

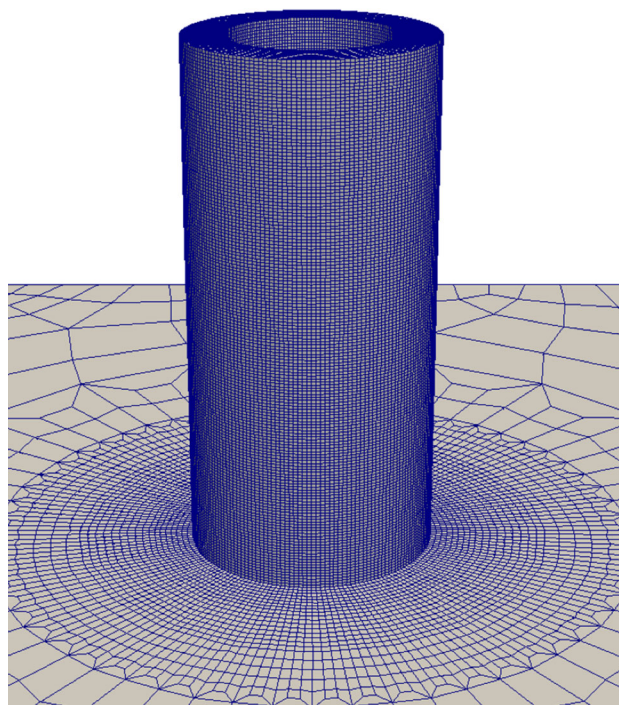


Fig. 2 Mesh of tube used in thermal FEA. The mesh consisted of 492,268 hexahedral elements

simulation. As in the thermal simulation, elements are activated once they reach the melting temperature. This work follows the quiet element approach [23], in which elements that have not yet reached melt are given a very low stiffness to prevent element inversion. Once the elements reach the melting temperature, they are given the true temperature-dependent material properties. The resulting thermal strain caused by thermal contraction produces a complex residual stress field to develop throughout the part. Note that the residual stress field evolves both during the additive manufacturing process and during the final cooldown. The strain caused by the process is a function of both mechanical strain and thermal strain

$$\epsilon_{total} = \epsilon_{mech} + \epsilon_{thermal} \quad (5)$$

The thermal strain is written as

$$\epsilon_{ij}^{thermal} = \alpha \Delta T \delta_{ij} \quad (6)$$

where α is the coefficient of thermal expansion, which was $1.96 \times 10^{-5} \text{ K}^{-1}$ [24]. The mechanical strain is governed by the equations below.

The constitutive model used in this work was the Bammann–Chiesa–Johnson (BCJ) isotropic elasto-viscoplastic internal state variable model. This model was originally developed based on work done by Bammann and Aifantis [25] and later updated by Brown and Bammann [26]

to include the effects of recrystallization. The model used here is a simplified version which is both temperature and history dependent, but does not include the effects of recrystallization. The model was calibrated to high temperature experimental data [27]. For the case of rate independent uniaxial tension, the stress evolves as

$$\dot{\sigma} = \left(\frac{\dot{E}}{E}\right)\sigma + E(\dot{\epsilon} - \dot{\epsilon}_p) \tag{7}$$

where E is the Young’s modulus, ϵ is the mechanical strain, and ϵ_p is the inelastic strain. Damage was not considered in this study, but the model can be extended to model damage evolution and failure [28]. The flow rule evolves according to

$$\dot{\epsilon}_p = f \sinh^n \left(\frac{\sigma_e - \kappa}{Y(T)} - 1 \right) \tag{8}$$

where Y is the rate independent initial yield stress, σ_e is the von Mises equivalent stress, T is the temperature, and κ is the isotropic hardening. The hardening variable κ evolves in a hardening minus recovery format as below:

$$\dot{\kappa} = \kappa \frac{\dot{\mu}}{\mu} + (H(T) - R_d(T)\kappa)\dot{\epsilon}_p \tag{9}$$

where H is the hardening modulus, and R_d is the dynamic recovery. The calibrated parameter set for the material model can be found in [27].

2.4 Microstructural prediction

Microstructure simulation was performed using a modified version of the Monte Carlo Potts model as described in [29–31]. A polycrystalline microstructure evolves under the Potts model by decreasing the microstructure’s total grain boundary energy through reduction of grain boundary surface area. The model achieves this by modifying sites in a simple cubic lattice along grain boundaries. Total system energy is calculated by summing over all sites with neighbors belonging to different grains. Each dissimilar pair is normalized to contribute unity to the total energy

$$E = \frac{1}{2} \sum_{i=1}^N \sum_{j=1}^L 1 - \delta(q_i, q_j) \tag{10}$$

where N is the total number of lattice sites, L is the number of neighbors at each site (26 here), and q_i is the grain identifier (or spin) at site i . Lattice sites change their grain membership to a neighboring value with probabilities determined by the Metropolis algorithm

$$P = \begin{cases} 1 & \text{for } \Delta E \leq 0 \\ \exp(-\Delta E/k_B T_{MC}) & \text{for } \Delta E > 0 \end{cases} \tag{11}$$

where ΔE the change in system energy resulting from a change and $k_B T_{MC}$ (0.6634 here) is the Monte Carlo temperature, which does not correspond to actual thermal temperature, but rather influences the stochastic roughness of the grain boundaries [32].

Two modifications to the Potts model are made to simulate microstructural evolution during solidification processes. First, molten behavior is simulated by randomizing any microstructures that exist in regions with a higher temperature than the specified melting point. Additionally, a temperature-dependent mobility term is added as a prefactor to the Metropolis algorithm:

$$M(T) = M_0 \exp\left(\frac{-Q}{RT}\right) \tag{12}$$

where M_0 is a prefactor (700 here), Q is the activation energy for grain boundary motion, and R is the gas constant (in these simulations, the ratio $Q/R = 12, 500$). $M(T)$ is implemented into Eq. (11) as

$$P = \begin{cases} M(T) & \text{for } \Delta E \leq 0 \\ M(T) \exp(-\Delta E/k_B T_{MC}) & \text{for } \Delta E > 0 \end{cases} \tag{13}$$

Implementing these modifications results in a model where significant evolution occurs in elevated temperature regions close to the melt pool, but decreases quickly with increasing distance. Thermal history was specified for each time step of the microstructure simulation by interpolating the corresponding thermal field from its finite element mesh to a regular cubic lattice. The interpolated field was then used to determine the corresponding grain boundary mobility field with Eq. (12). Lattice sites with temperatures greater than T_l were assumed to be molten, which is represented by randomizing any existing grain structure. Lattice sites are inactive until reaching T_l .

The current microstructure model predicts grain sizes and morphologies, but not crystallographic texture, formation of multiple phases, or porosity formation and evolution. Previous Monte Carlo-based models of microstructural evolution have incorporated these properties [33–35]. However, further work is required to implement them in additive manufacturing-specific simulations.

2.5 Experimental characterization

2.5.1 IR imaging

Radiance measurements were collected with a FLIR SC6700 mid-wave IR camera (640 × 512 pixel, InSb FPA) external to

the build chamber through a 2-in. inspection viewport loaded with a Ge window coated for 3–5 μm (Edmund Optics). This window transmits 97% of the mid-wave band but is highly absorptive at the laser wavelength ($> 10^4/\text{cm}$ at 1070 nm). A 0.25 in. extender mated to the 50 mm IR lens allowed for a $55 \times 44 \text{ mm}^2$ FOV at a working distance of $\sim 400 \text{ mm}$. To accommodate the 2 in. cylinder builds, the camera was mounted on its side. Data acquisition was triggered externally through a 5 V TTL signal from the Tormach controller board at the start of the builds. Two camera exposures were collected corresponding to two blackbody temperature ranges (523–873 and 773–1473 K) and later combined (super-framed). Cylinder builds acquired at 21 Hz generated $\sim 20 \text{ GB}$ of raw data in this configuration. Apparent temperatures were generated using the calculations within the FLIR software for atmospheric transmission, external optics transmission, and emissivity.

To compensate for the changing emissivity with temperature (and other surface effects such as roughness and oxidation), a procedure like that discussed in Dinwiddie et al. [36] was followed. A 304L block, approximately 1 in.³ was made at 500 W laser power and between 450–750 mm/s stage speed. This block was solid except for a deep cavity positioned at the center of one of the faces. The aspect ratio was such that this cavity acted as a blackbody with emissivity > 0.99 . Once fabricated, three K-type thermocouples (Omega) were inserted along the length of the cavity. The block was then placed on thin sheets of alumina silica ceramic (McMaster-Carr) while being heated by the defocused LENS laser beam ($\sim 9 \text{ mm}$ spot size). Short image sequences were captured with the FLIR from 573–1273 K in the same configuration as the cylinder builds. These images were analyzed to extract fits of the raw camera counts at each preset exposure to the extrapolated surface temperature read by the thermocouples, thus bypassing emissivity as a parameter to be entered. Finally, these calibration curves were used to convert the raw FLIR data from the cylinder builds to the apparent temperature values described in Sect. 3.1.

2.5.2 Electron backscatter diffraction

To examine the resultant microstructure from the LENS-built cylindrical tube, metallographic cross-sections were extracted and examined parallel to-, and perpendicular to-, the build direction. All cross-sections were metallographically polished to a 0.04 mm colloidal silica finish and imaged on a Zeiss SUPRA 55VP field emission scanning electron microscope (SEM) using electron backscatter diffraction (EBSD) for orientation imaging microscopy (OIM) [37,38]. This allowed for identification of individual grain morphologies and orientations as well as local and long range texture. An AZtec Electron backscatter diffraction (EBSD) system

Table 3 Summary of EBSD observation planes, their associated build heights and LENS power utilized at the given height

Transverse plane	Build height (mm above the base plate)	Height specific power (W)
1*	1.15	2000
2*	2.57	2000
3*	4.51	1750
4*	9.02	1500
5*	13.50	1250
6*	18.71	1250

was used for data collection with an indexing step size of 5 μm .

Regarding the planes of observation, along the build height, a single longitudinal cross-section spanning the base plate to the final build layers of the cylinder was examined first. This mounted EBSD map had a nominal area of $60 \times 6 \text{ mm}^2$. Following this initial scan, transverse sections were extracted perpendicular to the build direction at specific heights along the longitudinal map. The locations of these transverse planes are denoted by the nomenclature “1*”, “2*”, “3*”, “4*”, “5*” and “6*”. Each of these transverse scans contained the full wall thickness of the cylinder and spanned a nominal arc of 90° . The location of these transverse planes was selected due to its correspondence with a pronounced transition in the microstructure as revealed in the initial full height longitudinal map. In some cases, these microstructural transitions coincided with changes in laser power changes during the build. For a summary of the investigated transverse plane heights and their local delivered power, see Table 3.

3 Results and discussion

3.1 Thermal

The thermal simulations were executed on a high-performance computing (HPC) cluster using 240 cpus, and required approximately 8 h to complete. Images of the thermal simulations at three equally spaced times are shown in Fig. 3 below. The image at $t = 577 \text{ s}$ shows the completion of the final layer. As seen in this image, the majority of the part is above 1000 K. Figure 3 shows the effect of the Gaussian laser distribution on the hotspot. As expected, the hotspot possesses cooler temperatures at the edge of the build. The different layers can also be clearly seen throughout the build. The role of the base plate is also demonstrated in Fig. 3. Throughout the build, the bottom of the tube remains at a much lower temperature due to the base plate conducting heat out of the tube. This effect also shows the necessity

Fig. 3 Simulated temperature fields at three different times during the build. Time = 577 s corresponds to the completion of the final layer

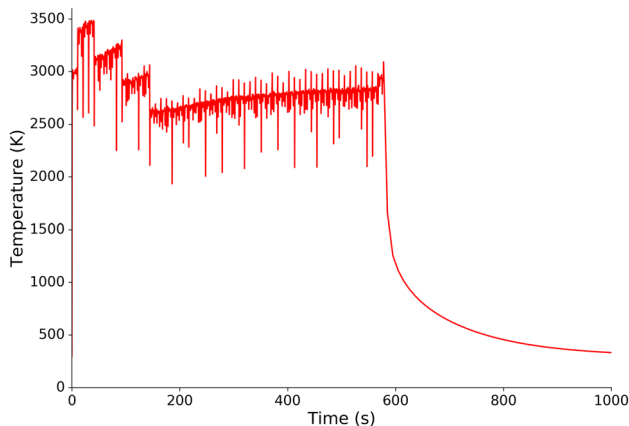
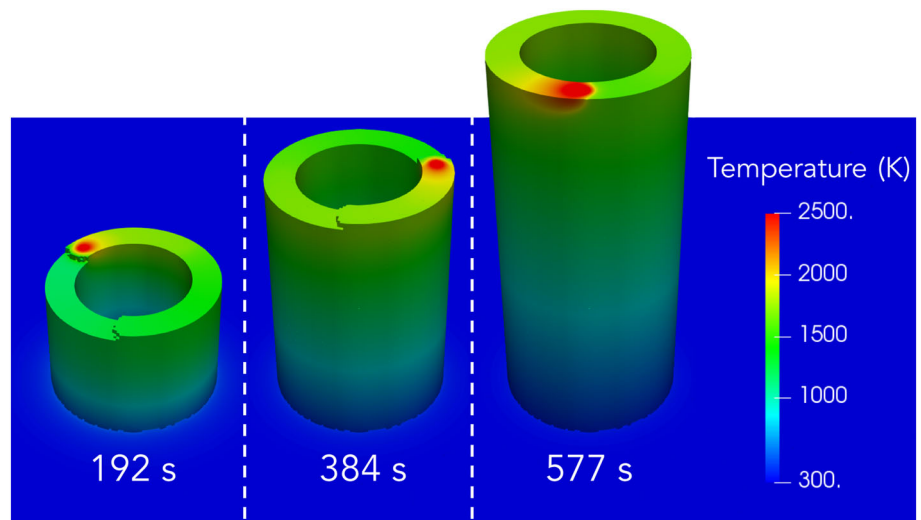


Fig. 4 Time history of maximum temperature across the build. The drops in temperature at the beginning of the build show the times at which the laser power was decreased

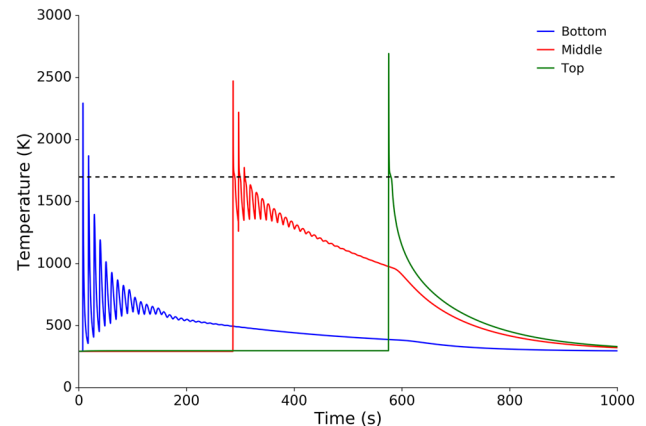


Fig. 5 Temperature history at locations at the bottom, middle, and top of the tube. The black dashed line represents the melting temperature. (Color figure online)

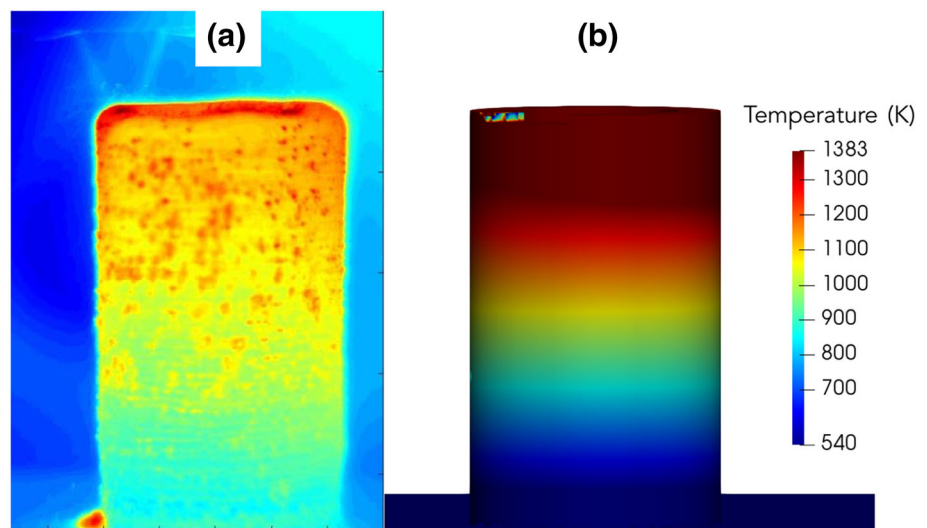
of the higher power near the baseplate to ensure sufficient adhesion. Although not obvious in the figure, elements on the outside edges of the first few layers never reached the melt temperature, and therefore were never activated. As the part builds, the thermal pathway to the baseplate is more limited, leading to a buildup of heat in the part. This observation was also made by the LENS operator, who noted that the tube was glowing red at the end of the build.

Figure 4 demonstrates the changes in peak overall temperature over time in the part. Early in the simulation, the periodic power decreases can be clearly seen by the drops in peak temperature, followed by a relatively stable region where the peak temperature remains in the range of 2500–3000 K for most of the build. Following the laser shutoff at 577s, the part cools back down to room temperature. Figure 5 shows temperature histories at three different locations corresponding to locations at the bottom, middle, and top of the part. For all three locations, the temperatures were taken

at the center of the wall thickness. The plots demonstrate the periodic nature of heating as subsequent layers are deposited. The plots also show that the layers undergo multiple remelting cycles. The bottom location is remelted once, and the middle location is remelted twice. As expected, the top layer does not undergo any remelting. The plots also show the large differences in thermal gradients during the build. Due to the previously mentioned buildup of heat, the middle location remains at an elevated temperature much longer than the bottom or top locations.

An IR image taken at 450 s is shown in Fig. 6 along with the temperature distribution of the simulation at the same time. The temperature scale is consistent for both images and matches the scale controlled by the IR measurement. In the middle of the temperature range, the comparative differences appear to be less than those at the extremes of the temperature range. The temperature gradients also look fairly similar in the middle of the temperature range.

Fig. 6 **a** Infrared image taken during build at $t = 450$ s, **b** simulation temperature distribution at $t = 450$ s



Above approximately 1200 K, the simulation appears to be over-predicting temperature, although there are significant questions regarding the accuracy of the IR images considering the area directly around the meltpool shows a maximum temperature of 1383 K, much lower than 304L's solidus temperature of 1673 K. The apparent temperatures from IR are highly dependent on the emissivity used in the conversion from raw counts to temperature. Emissivity has been shown to be highly dependent on surface roughness and oxidation [39], with reported literature values for 304L ranging from 0.17 to 0.9 [40,41]. Raplee et al. [42] observed changes in IR temperatures during an electron beam powder bed fusion build, which were attributed to surface swelling of the part and associated changes in radiation direction. The oxide layer that can sometimes form on the outer surface of the LENS parts will also affect IR measurements. Overcoming these issues still remains a challenge, and work is ongoing to provide more reliable quantitative measurements. Still, there are spots and regions on the IR image in the high temperature areas that appear to be in the same ranges of the simulation data, possibly hinting that the predictions are consistent, although this is hard to tell due to the rough surface finish and probable oxide layer on the LENS tube.

The temperatures shown in Fig. 6 are also much lower than the those in Fig. 4. One reason for this discrepancy is the previously described challenging nature of IR measurements. Another is that the IR image is taken orthogonal to the part build direction and likely does not see any of the actual meltpool, so these temperatures are not represented in the image. However, the plot in Fig. 4 is based on data from the simulation and can include temperatures from any point in the volume, including the meltpool.

3.2 Mechanical

The solid mechanics simulations were executed on a HPC cluster using 240 cpus, and required approximately 15 h to complete. The predicted residual von Mises stress after cooldown is shown in Fig. 7. As seen in the cross section of the tube, there is an extremely large stress gradient across the tube wall, with higher stresses on the outside. As expected, the stress is much higher near the baseplate compared to the top of the tube due to the constraint of the plate. Also, noticeable in the cross-section views is the reduced wall thickness at the base of the tube. This effect is caused by a reduced number of elements reaching melt temperature and activating. This effect was also observed experimentally and is caused by the cold baseplate acting as a large heat sink during the first layers of deposition. The effect of the large thermal mass of the baseplate limits the size of the melt pool, thereby leading to a smaller cross-section at the bottom of the tube. As the tube builds, the thermal pathway to the cool baseplate is longer and therefore more restrictive, resulting in a buildup of heat in the part and a larger melt pool. The top of the tube produces a high residual stress due to its higher thermal gradient, which has been shown to lead to higher residual stresses [43–45]. This gradient is illustrated by the rapid drop in temperature of the green curve in Fig. 5. Figure 7 also shows stresses that alternate between high and low values along the build height. These variations correspond to the locations of the successive layers, and are caused by the changing thermal boundary conditions over time.

The predicted axial stress after cooldown is shown in Fig. 8. Similar to the von Mises stress field, a gradient in axial stress exists across the thickness of the tube. Apart from the first several layers near the baseplate, the axial stress is mainly compressive on the outside surface of the tube. On

Fig. 7 Von Mises stress contours for **a** the outside surface of the tube and **b** a cross sectional view through the center of the tube. Note the vertical discontinuity in stress in **a** which corresponds to the location of where the laser moves vertically a layer height distance after completing each layer

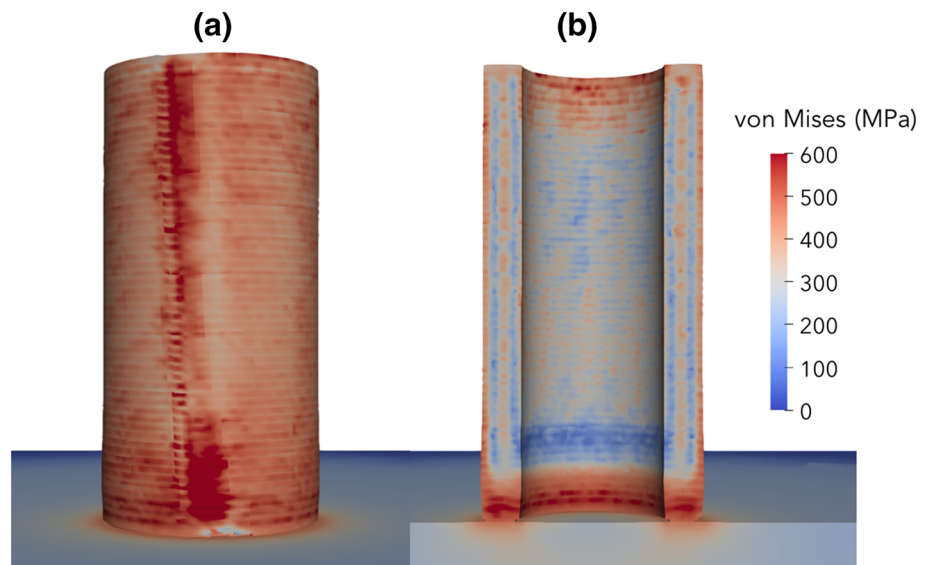
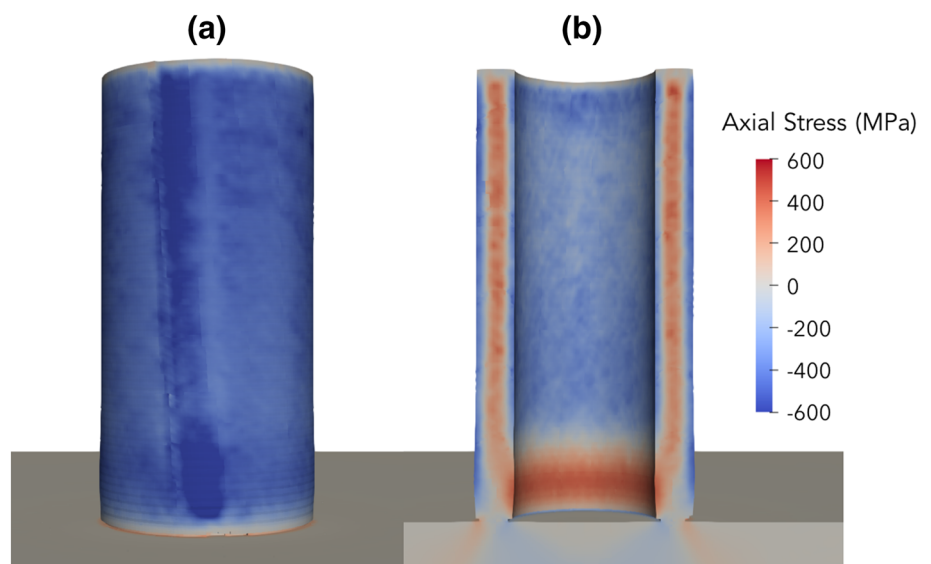


Fig. 8 Axial stress contours for **a** the outside surface of the tube and **b** a cross sectional view through the center of the tube. Note the through-thickness gradient in axial stress transitioning from compressive on the tube surfaces, both inner and outer, to tensile in the interior



the inside surface of the tube, regions of both tensile and compressive stresses exist.

Figure 9 illustrates the variation in maximum principal stresses across the part. Similar to the axial stress distribution, high tensile stresses occur in middle of the tube wall thickness, similar to a residual stress profile created by a quenching process in which the cooling propagates from the outside of the part inward. High tensile stresses also exist on the inner surface of the tube near the baseplate is due to a complex multiaxial stress state. Areas of high tensile stress could indicate locations of possible cracking during a build.

The residual stresses observed in the simulations were at or above yield for 304L, which is approximately 250 MPa [43]. Residual stresses near or above the room temperature material yield stress are not uncommon for AM materials [45–47], which illustrates the importance of considering

residual stress in AM parts. Figures 7 and 8 also show a vertical line of discontinuity in the stress values, which is a result of the LENS process. When the laser completes one circular layer scan, the platform the build is attached to moves vertically downward a distance of one layer thickness, and the next circular layer scan begins. This vertical shift causes a change in thermal gradients and affects the residual stress profile.

3.3 Microstructure

The microstructure simulations were performed on a single CPU core and required 15–96 h to complete depending on the number of time steps used. The final simulated microstructures are shown in Fig. 10. The images show that the microstructure transitioned from an equiaxed to colum-

Fig. 9 Maximum principal stress contours for **a** the outside surface of the tube and **b** a cross-sectional view through the center of the tube. Note the high tensile stresses in the center of the wall thickness and on the inside surface of the tube near the baseplate

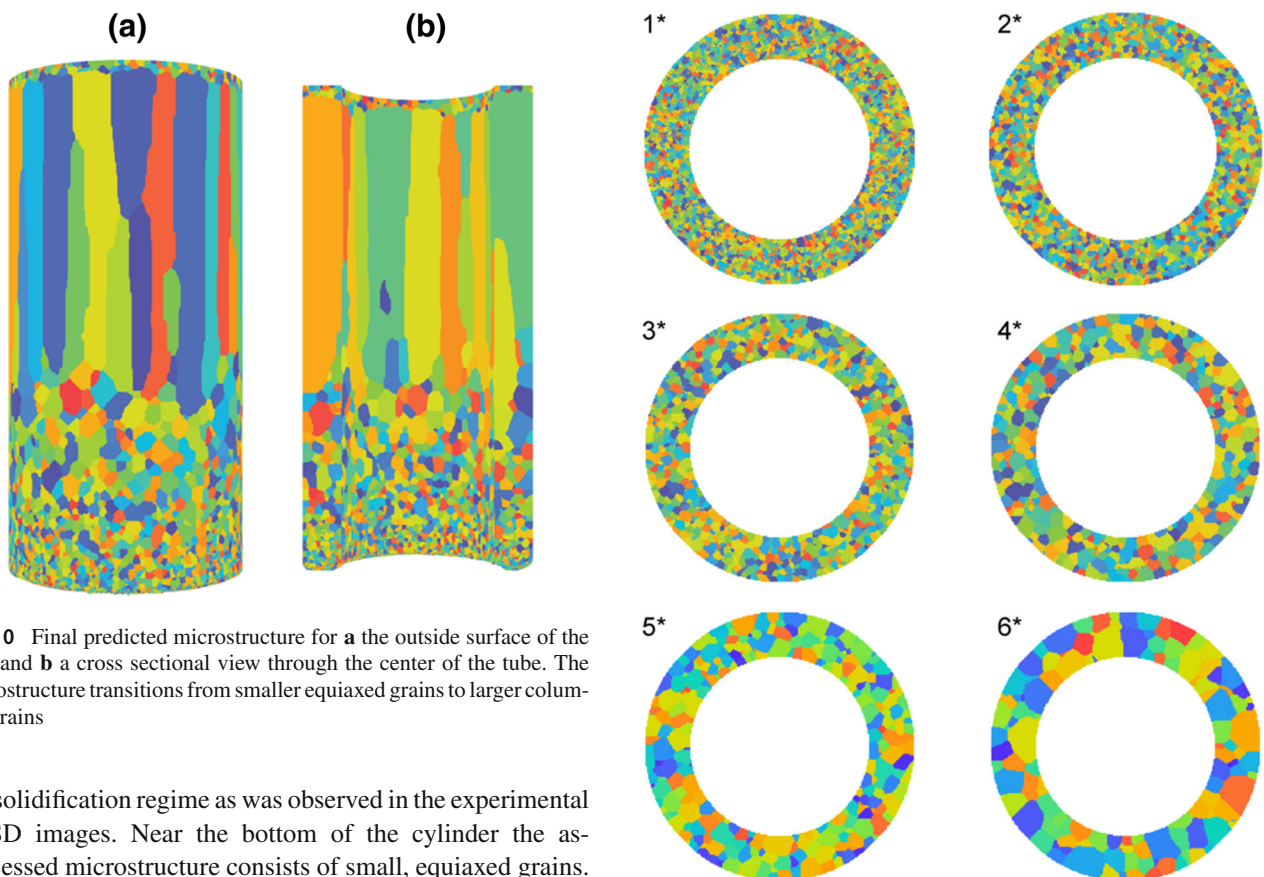
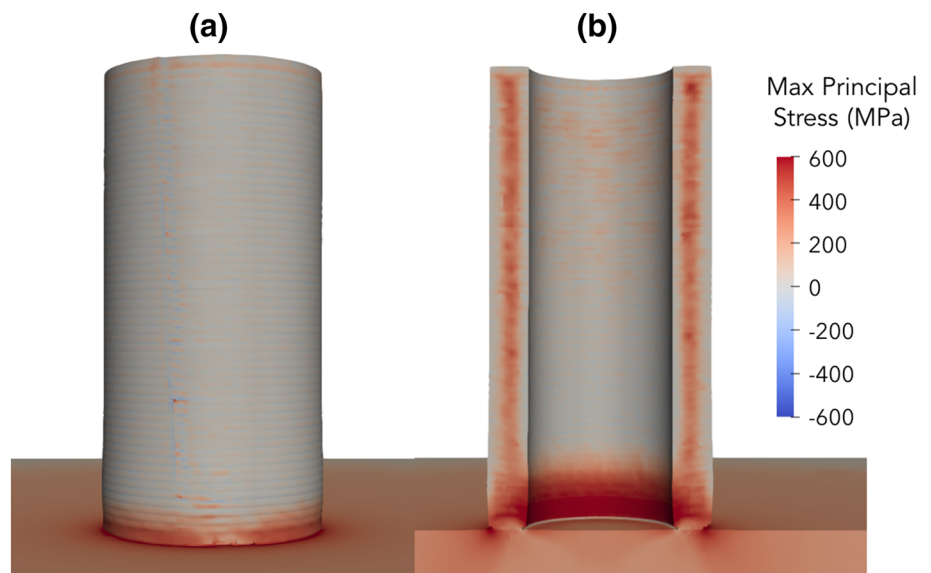


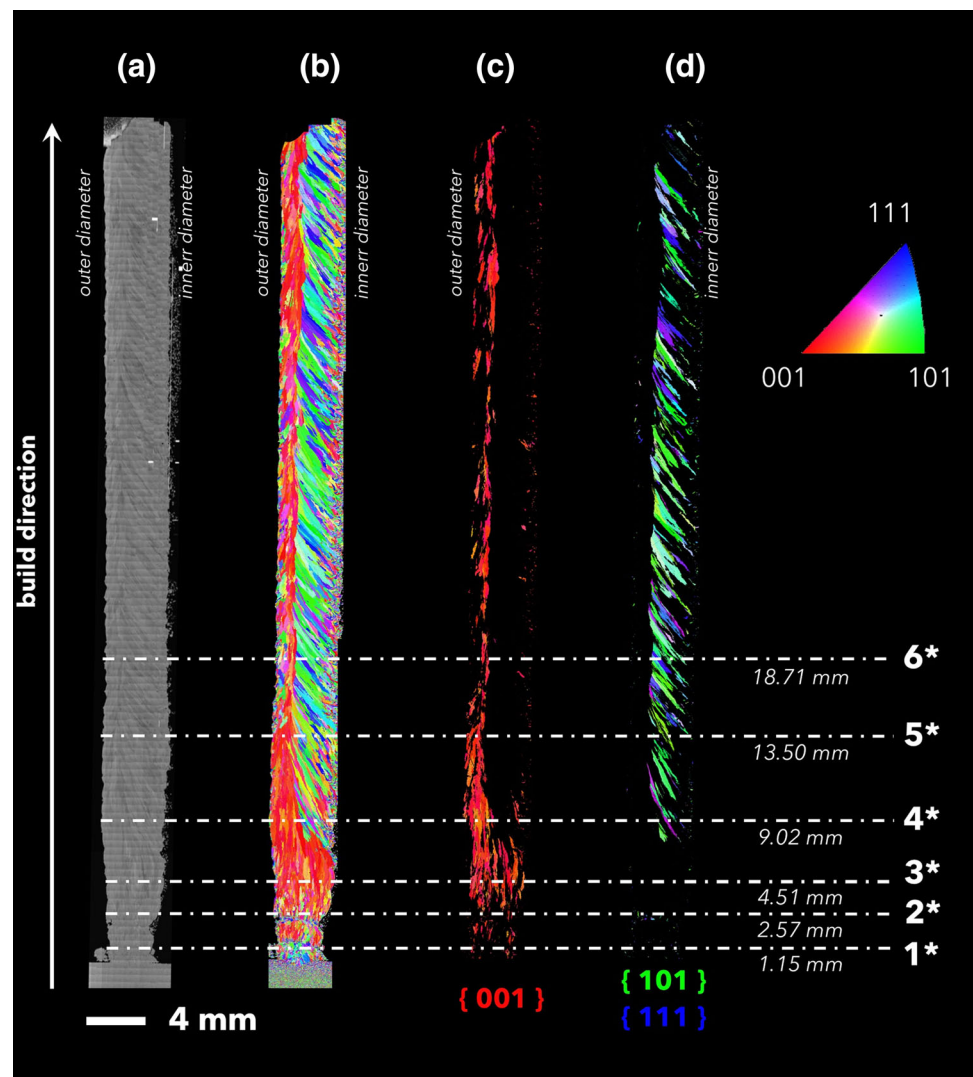
Fig. 10 Final predicted microstructure for **a** the outside surface of the tube and **b** a cross section through the center of the tube. The microstructure transitions from smaller equiaxed grains to larger columnar grains

nar solidification regime as was observed in the experimental EBSD images. Near the bottom of the cylinder the as-processed microstructure consists of small, equiaxed grains. With increasing height along the tube, the equiaxed grains grow larger. Approximately 28% along the height of the tube, the grain formation mechanism rapidly changes to a columnar growth mode. As the build continues, these grains grow competitively with each other until, in many regions, a single grain spans the entire wall thickness. At the very top of the tube, the grains are once again smaller and equiaxed. This occurs due to the lack of subsequent remelting by

Fig. 11 Transverse cross-sections of simulated microstructures at heights corresponding to experimental EBSD images

additional layers, and was also observed by Parimi et al. experimentally for a high power LENS build [48]. Transverse images (perpendicular to the build direction) of the microstructure simulations are shown in Fig. 11. The six cross-sections

Fig. 12 Grain Orientations along a longitudinal scan of an additively manufactured cylindrical domain. Colors denote crystallographic orientations as identified in the embedded inverse pole figure legend. Asterisked numbers indicate the heights at which transverse EBSD scans were subsequently obtained. (Color figure online)



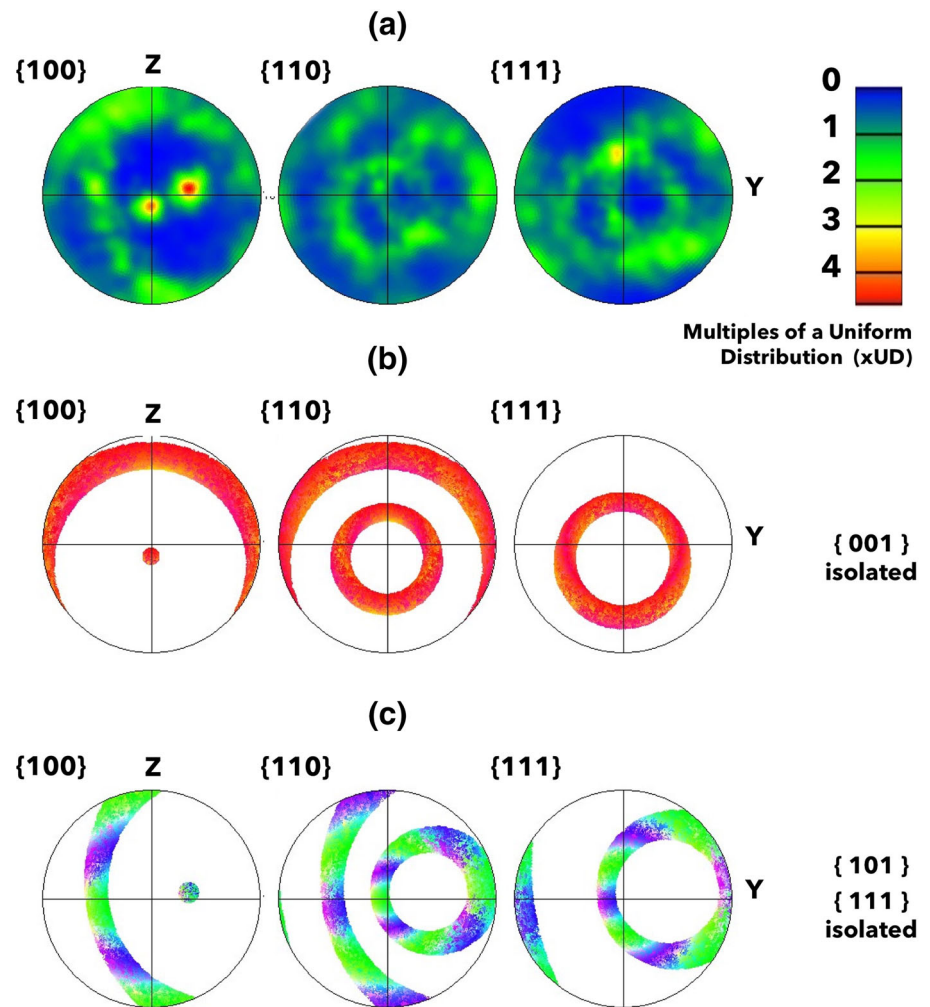
correspond to the experimental EBSD locations indicated in Figs. 12 and 14. The images show the gradual increase in grain size with increasing cross-section height. This increase in grain size corresponds to a decrease in the number of grains across the tube wall's width.

As mentioned previously, a longitudinal EBSD scan revealing the grain orientations present along the build height of the cylindrical body was acquired while six transverse scans perpendicular to the build direction were obtained subsequently. The resulting longitudinal EBSD scan with identifying planes for transverse scans are shown in Fig. 12. Here, grain colors correspond to their (001), (101) or (111) crystallographic orientations. In the fields of view shown, the exterior of the cylindrical body is located to the left and the interior of the cylindrical body is located to the right. Isolation imaging of the (001) and (101) + (111) grains are shown in the two visualizations immediately to the right of the primary longitudinal EBSD scan in Fig. 11c, d. The populations of the grain orientations present in Fig. 12 are revealed in the

standard stereographic projections shown in the topmost projections shown in Fig. 13a and are reported in multiples of a uniform distribution (\times UD). The center and lower series of standard projections in Fig. 13b, c correspond to the isolated crystallographic EBSD maps of Fig. 12. As can be seen, equiaxed grains are numerous at heights just above the build plate but soon transition to a significant quantity of columnar (001) grains beginning at 4.5 mm above the base plate. This collection of (001) grains continue to grow epitaxially across many layers and ultimately throughout the height of the entire build. Simultaneously, while the (001) grains become increasingly relegated to the vicinity near the external wall at 9 mm above the base plate, columnar grains possessing a mixture of (101) and (111) grains aligned at 45° to the build direction emerge and begin to account for approximately two-thirds of the grains located within each build layer.

The six transverse EBSD scans taken at select heights along the build direction are shown in Fig. 14. These scans

Fig. 13 Standard stereographic projections for the longitudinal EBSD scan shown in Fig. 12, indicating **a** the multiples of a uniform distribution associated with all crystallographic orientations observed, Fig. 12b, **b** the isolation of $\{001\}$ crystallographic families, Fig. 12c and **c** the isolation of $\{101\}$ and $\{111\}$ crystallographic families, Fig. 12d

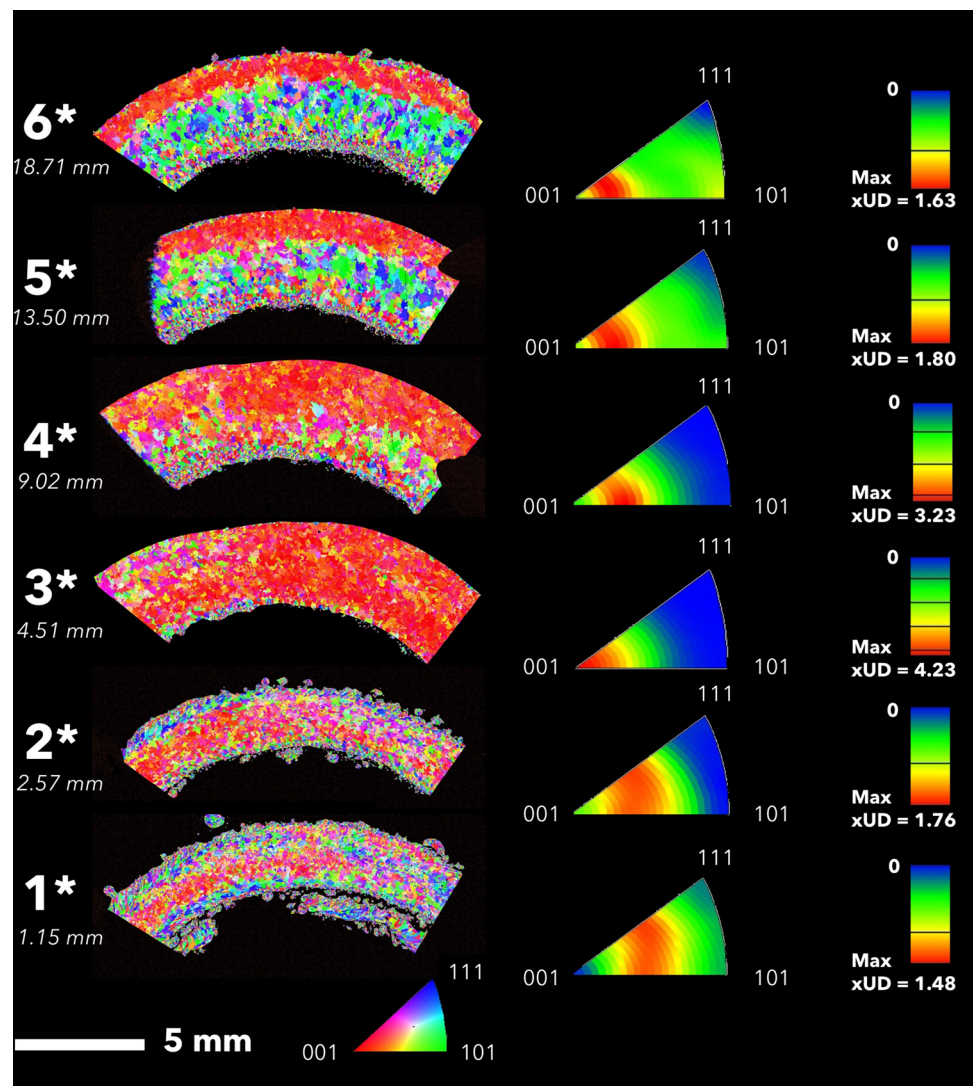


clearly corroborate the longitudinal observations of; (1) high populations of (001) textured grains existing throughout the height of the build near the external wall following the equiaxed to columnar transition at 2.57 mm above the base plate and (2) an increasing presence of mixed (101) and (111) grains with increasing height in the build. However, the inverse pole figures (IPFs) associated with each transverse section reveal the strength of the (001) grains reach up to 4 times the presence of any other orientation family at 4.5 mm above the build plate when nearly all grains in the transverse plane exhibited near (001) crystallographic orientations. The IPF maps also reveal two additional findings. The presence of equiaxed grains along the inner and outer surfaces of the cylinder walls do not occupy a significant portion of the grains revealed in transverse cross-sections for any heights greater than 2.5 mm above the build plate. Additionally, although columnar grains in the build direction are the dominant morphology for much of the cylindrical domain, in transverse, beginning at a height of 13.5 mm from the base plate, the build exhibits a strong tendency toward a more

uniform distribution of all grain orientations with a slightly lower concentration of (001) grains present. When combined with the results of the longitudinal scan, this appears to be a consistent arrangement for the remainder of the build.

There are several discrepancies between the experimental microstructures images of Figs. 12 and 14 and the simulated results of Figs. 10 and 11. The microstructure model recreates the equiaxed-to-columnar transition observed in the experiment, but fails to reproduce several of the finer-scale microstructural details including the grain heterogeneity shown in Fig. 12. Our previous modeling results were able to reproduce a similar microstructure for thin wall builds [29]. However, the microstructure simulations shown here utilized a small simulation domain to make the transfer and remeshing of the thermal model's results computationally tractable. This small domain resulted in a cubic lattice with unit lengths of 120 μm , larger than the average equiaxed grain size in the experimental results. This resolution is incapable of recreating the fine microstructural details observed in the experiments. Future work should enable a more effi-

Fig. 14 Transverse EBSD scans for increasing heights above the build plate within the additively manufactured cylindrical domain along with their respective quantitative inverse pole figures. Orientation populations are depicted by color scale bars shown at right using “multiples of a uniform distribution” (\times UD) as representative units. (Color figure online)



cient remeshing of the thermal model’s results and allow for much larger KMC domains resulting in more realistic microstructures.

It has been well understood for decades that fundamentally, grains grow in the direction of greatest heat extraction [49–51]. It is by this understanding that grain structures in welds [52], directional solidification [53] and single crystals [54,55] have been predicted, controlled and designed. In the grain structure of the tube, as seen in the EBSD results, the existence of a significant thermal gradient in the direction of the build is apparent in the abundance of (001) grains traversing nearly the entire build length. However, the abundance of (101) and (111) grains emanating from the interior sidewall at 45° suggests a competing thermal gradient whose effect on the layer by layer grain orientations rivals that which is being imposed by the conductive heating of the laser deposited material. This gradient is likely due to the uneven radiative and convective thermal conditions experienced within the

inner diameter of the cylindrical body versus its outer diameter. This cooling mismatch further supports the observation of asymmetric epitaxial columnar growth observed throughout the majority of the body’s longitudinal EBSD scan, see Fig. 12.

The exotic nature of the microstructure, which evolves from small equiaxed grains into a transition region of nearly all (001) grains into a region of angled columnar grains with a concentric ring of (001) grains throughout the length of the tube, presents a challenge for performance models. The areas of strong texture would have substantial effects on both the elastic and inelastic mechanical properties of the part. A standard homogeneous isotropic model would not be able to accurately predict behavior. Due to the different regions, the material is statistically heterogeneous, and would not lend itself well to general homogenization methods. Recent efforts at applying Direct Numerical Simulation (DNS) techniques have shown promise at capturing

the effects of microstructural variability in AM parts [56,57]. However, these techniques are computationally expensive for large parts. Work is ongoing to use statistical homogenization in different regions in conjunction with a posteriori error estimation techniques in order to facilitate recovery of local microstructural effects while using a simplified model, such as a macroscale anisotropic model [57]. Finally, the work presented here lends itself naturally to utilizing the thermal and microstructural histories in conjunction with a crystal plasticity model in order to predict type II, grain-specific residual stresses, which may be important for parts with small features and large grains. Work is also ongoing to develop this capability.

4 Conclusions

In this study, an additively manufactured build of a 304L stainless steel tube was simulated and compared to experiments. The thermal, structural, and microstructural histories were predicted with the goal of elucidating process-structure-property relationships. The thermal simulation results showed that in the first several layers, the base plate acts as a large heat sink and rapidly draws away heat. However, as the part builds, the overall temperature increases to the point where a large portion of the part, even many layers below the meltpool, are above 1000 K. The meltpool also descends into several pre-existing layers.

The structural simulations showed large values of residual stress at or above yield for 304L stainless steel. Even though the part is symmetric, stress gradients were found across the wall thickness. The residual stress also varied where the build platform moved vertically between layers, which produced a change in the local thermal gradient. This “step up” occurred in the same location in each layer and resulted in a vertical seam of higher stresses.

The microstructure demonstrated a transition from equiaxed to columnar grains, which was also predicted by the KMC simulations. This indicates that a steady state thermal condition was not reached until several layers were deposited. The location of the transition was also similar between prediction and experiment. While the simulations predicted regions of columnar grains, the predicted size of the columnar grains was much larger than what was observed with EBSD. We believe this is due to the relatively coarse grid size used in the simulation, which will be refined in future work.

Finally, asymmetric microstructures indicated that the centerline of the meltpool was offset towards the outer diameter of the tube, and was not aligned with the laser’s centerline. This offset indicates that the thermal losses at the surfaces corresponding to the inside and outside diameters of the cylinder are vastly different. These differences are likely

due to the fact that the inside surface is part of a nearly fully enclosed volume, which decreases radiative heat losses and limits convective flow. The grain structure offset is not present in the simulations because the thermal effects of the enclosed volume are neglected. Future work includes accounting for these differences in the thermal model and revisiting the microstructural predictions based on better informed local and long range thermal histories during the build.

Acknowledgements The authors would like to acknowledge Dave Keicher for support and development of the LENS process, Sam Subia, Tim Shelton, and the Sierra team for computational development and support, and Joe Michael, Alice Kilgo, Sara Dickens, Jay Carroll, and Philip Noell for EBSD work and fruitful discussions. Thoughtful reviews from Fadi Abdeljawad and Brad Trembacki are also greatly appreciated. Finally, the authors would like to acknowledge funding provided by the Born Qualified LDRD and thank Allen Roach (PI). Sandia National Laboratories is a multimission laboratory managed and operated by National Technology and Engineering Solutions of Sandia, LLC., a wholly owned subsidiary of Honeywell International, Inc., for the U.S. Department of Energy’s National Nuclear Security Administration under contract DE-NA0003525.

References

1. Frazier WE (2014) Metal additive manufacturing: a review. *J Mater Eng Perform* 23(6):1917–1928
2. Shamsaei N, Yadollahi A, Bian L, Thompson SM (2015) An overview of Direct Laser Deposition for additive manufacturing; part II: mechanical behavior, process parameter optimization and control. *Addit Manuf* 8:12–35
3. Thompson SM, Bian L, Shamsaei N, Yadollahi A (2015) An overview of Direct Laser Deposition for additive manufacturing; part I: transport phenomena, modeling and diagnostics. *Addit Manuf* 8:36–62
4. Ding D, Pan Z, Cuiuri D, Li H (2015) Wire-feed additive manufacturing of metal components: technologies, developments and future interests. *Int J Adv Manuf Technol* 81(1–4):465–481
5. Keicher DM, Smugeresky JE, Romero JA, Griffith ML, Harwell LD (1997) Using the laser engineered net shaping (LENS) process to produce complex components from a CAD solid model, pp 91–97
6. Bourell DL, Rosen DW, Leu MC (2014) The roadmap for additive manufacturing and its impact. *3D Print Addit Manuf* 1(1):6–9
7. Withers PJ (2007) Residual stress and its role in failure. *Rep Prog Phys* 70(12):2211–2264
8. Hodge NE, Ferencz RM, Solberg JM (2014) Implementation of a thermomechanical model for the simulation of selective laser melting. *Comput Mech* 54(1):33–51
9. Pal D, Patil N, Zeng K, Stucker B (2014) An integrated approach to additive manufacturing simulations using physics based, coupled multiscale process modeling. *J Manuf Sci Eng* 136(6):061022
10. Denlinger ER, Irwin J, Michaleris P (2014) Thermomechanical modeling of additive manufacturing large parts. *J Manuf Sci Eng* 136(6):061007
11. Francois MM et al (2017) Modeling of additive manufacturing processes for metals: challenges and opportunities. *Curr Opin Solid State Mater Sci* 21:198–206
12. Smith J et al (2016) Linking process, structure, property, and performance for metal-based additive manufacturing: computational

- approaches with experimental support. *Comput Mech* 57(4):583–610
13. Goldak J, Chakravarti A, Bibby M (1984) A new finite element model for welding heat sources. *Metall Trans B* 15(2):299–305
 14. Dehoff RR, Kirka MM, List FA, Unocic KA, Sames WJ (2015) Crystallographic texture engineering through novel melt strategies via electron beam melting: Inconel 718. *Mater Sci Technol* 31(8):939–944
 15. Bontha S, Klingbeil NW, Kobryn PA, Fraser HL (2009) Effects of process variables and size-scale on solidification microstructure in beam-based fabrication of bulky 3D structures. *Mater Sci Eng A* 513–514:311–318
 16. Vastola G, Zhang G, Pei QX, Zhang Y-W (2016) Erratum to: modeling the microstructure evolution during additive manufacturing of Ti6Al4V: a comparison between electron beam melting and selective laser melting. *JOM* 68(8):2296–2296
 17. Kelly SM, Kampe SL (2004) Microstructural evolution in laser-deposited multilayer Ti-6Al-4V builds: part II. Thermal modeling. *Metall Mater Trans A* 35(6):1869–1879
 18. SIERRA Solid Mechanics Team 2017, Sierra/SolidMechanics 4.44 user guide, SAND2017-3771. Sandia National Laboratories
 19. Plimpton SJ et al (2009) Crossing the mesoscale no-mans land via parallel kinetic Monte Carlo. SAND2009-6226, 966942
 20. Roters F, Eisenlohr P, Hantcherli L, Tjahjanto DD, Bieler TR, Raabe D (2010) Overview of constitutive laws, kinematics, homogenization and multiscale methods in crystal plasticity finite-element modeling: theory, experiments, applications. *Acta Mater* 58(4):1152–1211
 21. Heigel JC, Michaleris P, Reutzel EW (2015) Thermo-mechanical model development and validation of directed energy deposition additive manufacturing of Ti-6Al-4V. *Addit Manuf* 5:9–19
 22. Denlinger ER, Jagdale V, Srinivasan GV, El-Wardany T, Michaleris P (2016) Thermal modeling of Inconel 718 processed with powder bed fusion and experimental validation using in situ measurements. *Addit Manuf* 11:7–15
 23. Michaleris P (2014) Modeling metal deposition in heat transfer analyses of additive manufacturing processes. *Finite Elem Anal Des* 86:51–60
 24. Rai R, Elmer JW, Palmer TA, DebRoy T (2007) Heat transfer and fluid flow during keyhole mode laser welding of tantalum, Ti-6Al-4V, 304L stainless steel and vanadium. *J Phys D Appl Phys* 40(18):5753–5766
 25. Bammann DJ, Aifantis EC (1987) A model for finite-deformation plasticity. *Acta Mech* 69(1–4):97–117
 26. Brown AA, Bammann DJ (2012) Validation of a model for static and dynamic recrystallization in metals. *Int J Plast* 32–33:17–35
 27. Jamison RD et al (2017) Validation of a glass-to-metal seal finite-element model. Sandia National Laboratories, Albuquerque, NM, SAND2017-10894
 28. Karlson KN, Foulk JW, Brown AA, Veilleux MG (2016) Sandia fracture challenge 2: Sandia California’s modeling approach. *Int J Fract* 198(1–2):179–195
 29. Rodgers TM, Madison JD, Tikare V (2017) Simulation of metal additive manufacturing microstructures using kinetic Monte Carlo. *Comput Mater Sci* 135:78–89
 30. Rodgers TM, Madison JD, Tikare V, Maguire MC (2016) Predicting mesoscale microstructural evolution in electron beam welding. *JOM* 68(5):1419–1426
 31. Popova E, Rodgers TM, Gong X, Cecen A, Madison JD, Kalidindi SR (2017) Process-structure linkages using a data science approach: application to simulated additive manufacturing data. *Integr Mater Manuf Innov* 6(1):54–68
 32. Zöllner D (2014) A new point of view to determine the simulation temperature for the Potts model simulation of grain growth. *Comput Mater Sci* 86:99–107
 33. Zhang L, Rollett AD, Bartel T, Wu D, Lusk MT (2012) A calibrated Monte Carlo approach to quantify the impacts of misorientation and different driving forces on texture development. *Acta Mater* 60(3):1201–1210
 34. Holm EA, Srolovitz DJ, Cahn JW (1993) Microstructural evolution in two-dimensional two-phase polycrystals. *Acta Metall Mater* 41(4):1119–1136
 35. Tikare V, Braginsky M, Bouvard D, Vagnon A (2010) Numerical simulation of microstructural evolution during sintering at the mesoscale in a 3D powder compact. *Comput Mater Sci* 48(2):317–325
 36. Dinwiddie RB, Kirka MM, Lloyd PD, Dehoff RR, Lowe LE, Marlow GS (2016) Calibrating IR cameras for in-situ temperature measurement during the electron beam melt processing of Inconel 718 and Ti-Al6-V4, p 986107
 37. Dingley D (2004) Progressive steps in the development of electron backscatter diffraction and orientation imaging microscopy: EBSD AND OIM. *J Microsc* 213(3):214–224
 38. Schwarzer RA, Field DP, Adams BL, Kumar M, Schwartz AJ (2009) Present state of electron backscatter diffraction and prospective developments. In: Schwartz AJ, Kumar M, Adams BL, Field DP (eds) *Electron backscatter diffraction in materials science*. Springer, Boston, pp 1–20
 39. Sridharan K, Allen T, Anderson M, Cao G, Kulcinski G (2011) Emissivity of candidate materials for VHTR applications: role of oxidation and surface modification treatments. *DOE/ID/14820, 1022709*
 40. Zhu X, Chao Y (2004) Numerical simulation of transient temperature and residual stresses in friction stir welding of 304L stainless steel. *J Mater Process Technol* 146(2):263–272
 41. Gery D, Long H, Maropoulos P (2005) Effects of welding speed, energy input and heat source distribution on temperature variations in butt joint welding. *J Mater Process Technol* 167(2–3):393–401
 42. Raplee J et al (2017) Thermographic microstructure monitoring in electron beam additive manufacturing. *Sci Rep* 7:43554
 43. Vasinonta A, Beuth JL, Griffith M (2007) Process maps for predicting residual stress and melt pool size in the laser-based fabrication of thin-walled structures. *J Manuf Sci Eng* 129(1):101
 44. Vasinonta A, Beuth JL, Griffith ML (2000) Process maps for controlling residual stress and melt pool size in laser-based SFF processes. Presented at the solid freeform fabrication symposium, Austin, TX
 45. Aggarangsi P, Beuth JL (2006) Localized preheating approaches for reducing residual stress in additive manufacturing. Presented at the solid freeform fabrication symposium, Austin, TX, pp 709–720
 46. Mercelis P, Kruth J (2006) Residual stresses in selective laser sintering and selective laser melting. *Rapid Prototyp J* 12(5):254–265
 47. Knowles C, Becker T, Tait R (2012) Residual stress measurements and structural integrity implications for selective laser melted Ti-6Al-4V. *S Afr J Ind Eng* 23(3):119
 48. Parimi LL, Ravi GA, Clark D, Attallah MM (2014) Microstructural and texture development in direct laser fabricated IN718. *Mater Charact* 89:102–111
 49. Copley SM, Giamei AF, Johnson SM, Hornbecker MF (1970) The origin of freckles in unidirectionally solidified castings. *Metall Trans* 1(8):2193–2204
 50. Flemings MC (1974) Solidification processing. *Metall Trans* 5(10):2121–2134
 51. Versnyder FL, Shank ME (1979) Role of directional solidification. In: Bradley EF (ed) *Source book on materials for elevated-temperature applications*. American Society for Metals, Metals Park, pp 334–368
 52. Ashby MF, Easterling KE (1982) A first report on diagrams for grain growth in welds. *Acta Metall* 30(11):1969–1978
 53. Elliott AJ, Pollock TM, Tin S, King WT, Huang S-C, Gigliotti MFX (2004) Directional solidification of large superalloy castings

- with radiation and liquid-metal cooling: a comparative assessment. *Metall Mater Trans A* 35(10):3221–3231
54. Madison J, Spowart J, Rowenhorst D, Aagesen LK, Thornton K, Pollock TM (2010) Modeling fluid flow in three-dimensional single crystal dendritic structures. *Acta Mater* 58(8):2864–2875
55. Madison J, Spowart JE, Rowenhorst DJ, Aagesen LK, Thornton K, Pollock TM (2012) Fluid flow and defect formation in the three-dimensional dendritic structure of nickel-based single crystals. *Metall Mater Trans A* 43(1):369–380
56. Bishop JE, Emery JM, Battaile CC, Littlewood DJ, Baines AJ (2016) Direct numerical simulations in solid mechanics for quantifying the macroscale effects of microstructure and material model-form error. *JOM* 68(5):1427–1445
57. Brown JA, Bishop JE (2016) Quantifying the impact of material-model error on macroscale quantities-of-interest using multiscale a posteriori error-estimation techniques. *MRS Adv* 1(40):2789–2794
58. Bogaard RH, Desai PD, Li HH, Ho CY (1993) Thermophysical properties of stainless steels. *Thermochim Acta* 218:373–393